

Accepted Author Manuscript of

Margit Fabian, Istvan Tolnai, Atul Khanna, Zsolt Endre Horvath, Viktoria Kovacs Kis, Zsolt Kovacs, *physica status solidi (a)* applications and materials science, DOI: 10.1002/pssa.202000682

Structural Characterization of Oxy-Halide Materials for Solid State Batteries

Margit Fabian^{1*}, Istvan Tolnai¹, Atul Khanna², Zsolt Endre Horvath¹, Viktoria Kovacs Kis¹, Zsolt Kovacs³

¹Centre for Energy Research, 1121 Budapest Konkoly Thege st 29-33, Hungary

²Department of Physics, Guru Nanak Dev University, Amritsar-143005, India

³Department of Materials Physics, Eötvös Loránd University, H-1117 Budapest, Pázmány Péter sétány 1/a, Hungary

Corresponding author: fabian.margit@ek-cer.hu

Keywords: oxy-halides, neutron and X-ray diffraction, Reverse Monte Carlo simulation, thermal properties, TEM morphology

Abstract

Development of new materials with novel composition to obtain rechargeable solid state batteries with improved capacity and energy density is one of the hot topics in material science. Inorganic and thermally stable oxy-halide materials are potential substitutes for the toxic and flammable organic liquid electrolytes that are used in the Li-ion batteries. In this work, applying multi-steps heat treatment, Li-, Na- and K-ion based oxy-halide materials doped with Ca, Ba and Mg has synthesized. The samples have been characterized by neutron and X-ray diffractometry, Raman spectroscopy, thermal analysis and transmission electron microscopy.

Significant differences can be observed between the Li/Na/K-series, but within the series the diffraction character of the compositions is similar, a semi-amorphous/crystalline phase were identified. Characteristic first and second neighbor distributions reveal a very compact network structure. X-ray diffractometry and Raman studies proved that the investigated Li, Na and K-based samples absorb water, even if they were kept under dry conditions. The Li₃OCl anti-perovskite phase was identified by XRD in for all the Ca-, Ba- and Mg-doped samples. TEM studies show that the morphology of the samples consists of nanograins of different size below 100 nm. According to elemental maps, the doping Ba forms oxide nanoparticles, while Mg is incorporated into the Na- and K-based network structure.

1. Introduction

Reduction of the dependence of modern society on fossil fuels is an urgent issue. To be able to replace fossil fuels by alternative energy sources like wind or solar energy, the storage of electric power from these renewable sources in rechargeable batteries should be solved. Nowadays the most common rechargeable batteries are alkali metal-ion batteries [1, 2], which

have been extensively studied since 1970s. Li-ion batteries were invented by John Goodenough about 30 years ago (the significance of this scientific and technological breakthrough was reflected by the 2019 Nobel Prize in Chemistry) however, the safety of these batteries remains a barrier for their application in high power systems such as smart electronic systems or electric cars. Particularly, modern Li-batteries have safety problems and narrow operating temperature ranges. Thus, currently they cannot meet the growing demand for higher energy storage density, charging speed and cost reduction and, further improvements in their design and operation are needed [3]. Besides lithium-ion batteries, sodium-ion batteries have also been rapidly developed recently, thanks to the fact that sodium is cheaper than lithium and widely available from the oceans. Based on the Nobel-laureate Goodenough's – idea [1, 2] the new type of glasses/amorphous solids is a potential candidate for preparing all solid-state, safe and rechargeable batteries with high ionic conductivity, energy density and long duration thermal and chemical stability [4-7]. The open structure of inorganic glassy materials facilitates the process of ionic hopping and results in enhanced conductivity. The amorphous oxy-halides are derived from crystalline metal hydroxide precursors ($\text{Ba}(\text{OH})_2$, $\text{Ca}(\text{OH})_2$, $\text{Mg}(\text{OH})_2$) and have the highest reported Li^+ and Na^+ conductivity ($\sigma > 10^{-2} \text{ S cm}^{-1}$ at room temperature; 25 °C).

Our work is mainly focuses on the development and structural characterization of a solid amorphous Li^+ or Na^+ or K^+ electrolytes doped with Ca, Ba and Mg, allowing the fast charging of the battery without the formation of metal dendrites (dendrites can produce an internal short-circuit, which results in thermal runaway and ignition of the flammable liquid electrolyte) [6,8-10]. In spite of the very promising properties of Li/Na/K-based electrolytes, their structural properties are still not well understood. In this work we study the structural details and properties of these materials, in relation with ionic conductivity.

The Li^+ , Na^+ and K^+ -based superionic oxy-halide solids/glasses were synthesized by heat treatment. In order to get deeper insight into the network structure, we have undertaken neutron- and X-ray diffraction studies combined with Raman spectroscopy and transmission electron microscopy. The structure of the materials was correlated with thermal stability. As the ionic conductivity in an amorphous solid (glass) occurs through a hopping mechanism, and it is essential to understand the local structure to predict and modify the ionic conductivity and the energy storage capacity.

2. Experimental

2.1. Sample preparation

Li-, Na- and K-ion based oxy-halides materials with nominal compositions: $\text{A}_{3-2x}\text{M}_x\text{O}_{1+y}\text{Cl}_{1-2y}$ (where A=Li, Na, K; M=Ca, Ba, Mg; $x=0.005$; $y=0$) have been prepared taken based on the receipt from Ref [11]. The samples are $\text{Li}_{2.99}\text{Ca}_{0.005}\text{OCl}$, $\text{Li}_{2.99}\text{Ba}_{0.005}\text{OCl}$ and $\text{Li}_{2.99}\text{Mg}_{0.005}\text{OCl}$ (hereafter referred to as $\text{Li}_3\text{OCl-Ca}$, $\text{Li}_3\text{OCl-Ba}$ and $\text{Li}_3\text{OCl-Mg}$), $\text{Na}_{2.99}\text{Ca}_{0.005}\text{OCl}$, $\text{Na}_{2.99}\text{Ba}_{0.005}\text{OCl}$ and $\text{Na}_{2.99}\text{Mg}_{0.005}\text{OCl}$ (hereafter referred to as $\text{Na}_3\text{OCl-Ca}$, $\text{Na}_3\text{OCl-Ba}$ and $\text{Na}_3\text{OCl-Mg}$) and $\text{K}_{2.99}\text{Ca}_{0.005}\text{OCl}$, $\text{K}_{2.99}\text{Ba}_{0.005}\text{OCl}$ and $\text{K}_{2.99}\text{Mg}_{0.005}\text{OCl}$ (hereafter referred to as $\text{K}_3\text{OCl-Ca}$, $\text{K}_3\text{OCl-Ba}$ and $\text{K}_3\text{OCl-Mg}$). Analytical grade, LiCl, NaCl, KCl, NaOH, $\text{Ca}(\text{OH})_2$, $\text{Ba}(\text{OH})_2$, $\text{Mg}(\text{OH})_2$ commercial powders (purchased from VWR International Company) were used to prepare the samples. The raw materials were pre-dried, the stoichiometric amounts were weighted and the weighted materials were mixed and homogenized. Batch mixture were

melted in a closed Teflon crucible in a suitable electrical furnace at 250°C. The solidified bulk samples were comminuted by ball-milling, using agate balls to a particle size below 50 μm . As most of the mixtures were highly hygroscopic, the samples were handled in glove-box under inert (N_2) atmosphere during sample preparation.

2.2. X-ray diffractometry

X-ray diffraction (XRD) measurements were performed using a Bruker AXS D8 Discover diffractometer equipped with Göbel-mirror and a scintillation detector with $\text{Cu K}\alpha$ ($\lambda=1.5406$ Å) radiation. The X-ray beam dimensions were 1 mm * 5 mm, the 2θ step size was 0.02 °, $2\theta=10-60$ °, scan speed 0.3 °/min. The samples were covered by Scotch tape in order to protect them from air during measurement. We used the Diffrac.EVA program and the ICDD PDF database for phase identification.

2.3. Raman spectroscopy

Renishaw In-Via Reflex micro-Raman spectrometer was used to measure the Raman spectra of the samples by using an Ar-ion laser of 488 nm excitation wavelength (50 mW). Measurements were performed in an unpolarized mode at room temperature in the back-scattering geometry in the wave number range of 30 to 1100 cm^{-1} at a spectral resolution of $\sim 1\text{cm}^{-1}$. The spectra acquisition time was at average 3 minutes/sample.

2.4. Neutron diffractometry

Neutron diffraction (ND) experiments were performed at 100 °C temperature by using monochromatic neutrons ($\lambda_0=1.068$ Å) [12] at the 2-axis PSD diffractometer of Budapest Neutron Centre in the momentum transfer range $Q=0.45-10$ Å $^{-1}$. The powder specimens of about 3–4 g/each were filled in thin walled cylindrical vanadium sample holder of 6 mm diameter, and put into a TiZr null matrix alloy in-situ cell (Ti-Zr alloy in atomic ratio 52.2:47.5 is non-scattering for neutrons). Data were corrected for detector efficiency, background scattering and absorption effects. The total structure factor, $S(Q)$ was calculated by local software packages.

2.5. Thermal characterization

For differential thermal analysis (DTA), 50-70 mg powder samples were weighted in glove box, under high purity (5N) Ar atmosphere (O_2 level was lower than 0.7 at%) and transported to the DTA equipment in the same environment. For accurate mass measurements the samples were open to air and then placed into the DTA equipment and depressurized by a rotary pump. This period in air took about 1 min for each samples. Subsequently, DTA measurements were performed using a SETARAM 92-16.18 DTA equipment with a TGA-92 setup under Ar atmosphere. The DTA was calibrated by melting of high purity In, Zn and Al metals and each DTA scan consisted of a controlled heating with 5 °C/min constant heating rate between room temperature and 400 °C and a subsequent instantaneous uncontrolled cooling of the sample. Maximum uncertainty in the measurement of glass transition, crystallization and melting temperatures is $\pm 1^\circ\text{C}$.

2.6. Electron microscopy and electron diffraction

For high resolution transmission electron microscopy (HRTEM) and electron diffraction (ED), the sample was gently crushed under ethanol in an agate mortar, and a drop of the resulting suspension was deposited onto a lacey carbon covered Cu grid (Ted Pella). TEM analysis was performed using an FEI Titan-Themis 200 G3 transmission electron microscope with a C_s corrected objective lens, (point resolution ~ 0.09 nm in image mode and 0.16 nm in scanning transmission electron microscopy (STEM) mode) operated at 200 kV. The TEM is equipped with FEI Super-X energy dispersive X-Ray spectroscopy (EDS) detection system which allows EDS point measurements in when operating in TEM mode and EDS mapping in STEM mode. Bright field images, selected area electron diffraction (SAED) patterns and EDS were made using a Philips CM20 TEM. SAED patterns were taken from areas of ca. 1 μm and 250 nm of diameter. Interplanar spacing values were calculated based on the position of the observed diffraction rings. EDS analysis was made using a nominal electron beam size 55 nm.

3. Results and discussion

Figure 1 represents the X-ray diffraction intensities of the investigated samples. The formation of anti-perovskite Li_3OCl is verified by X-ray diffractometry. As shown in Figure 1a, the peak at $2\theta=32.7^\circ$ can be indexed as (011) of the cubic Li_3OCl phase with the space group of $Pm\bar{3}m$ and lattice constant of 3.91 \AA (the crystal structure of cubic Li_3OCl can be seen in the inset in Figure 1a) [13]. Besides the anti-perovskite phase, the LiCl , Li_2CO_3 , $\text{LiCl}(\text{H}_2\text{O})$ and $\text{Li}_4\text{Cl}(\text{OH})_3$ phases were identified. The $\text{LiCl}(\text{H}_2\text{O})$ and $\text{Li}_4\text{Cl}(\text{OH})_3$ phases demonstrate the water absorption by LiCl while Li_2CO_3 can be the consequence of CO_2 uptake from air.

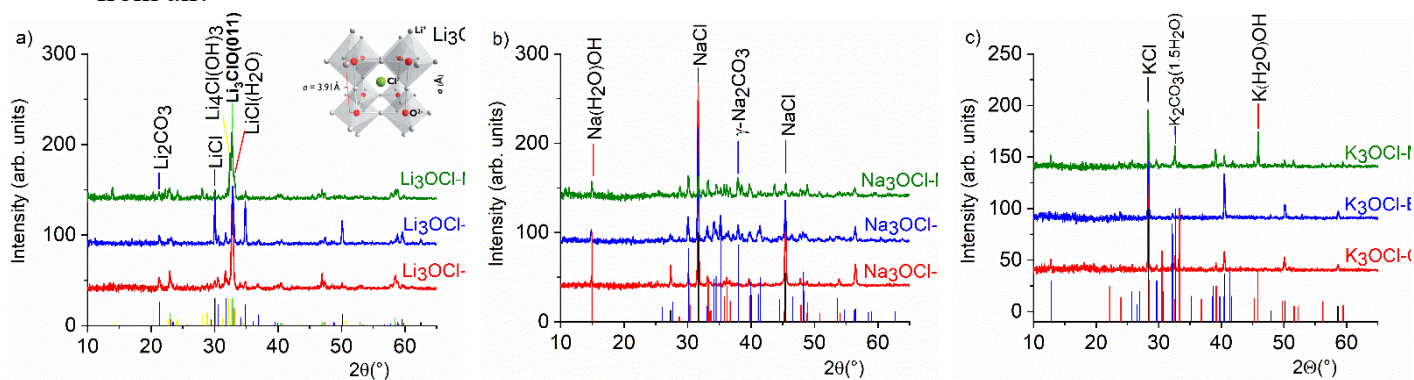


Figure 1. X-ray diffraction patterns of Li_3OCl -Ca/Ba/Mg (a), Na_3OCl -Ca/Ba/Mg (b) and K_3OCl -Ca/Ba/Mg (c) samples collected at room temperature.

In the Na-based samples the NaCl , as well as $\gamma\text{-Na}_2\text{CO}_3$ and $\text{NaOH}\cdot\text{H}_2\text{O}$ phases can be identified the latter one proves again water uptake. NaClO_4 phase formation can be observed only in the case of Na_3OCl -Ca sample. In the case of the Na_3OCl -Mg sample, no phase(s) could be assigned to some of the diffraction peaks unambiguously based on the present measurements which suggest that besides the above mentioned compounds we probably have a more complex structure. In the K-based sample, three phases KCl , $\text{K}(\text{H}_2\text{O})\text{OH}$ and $\text{K}_2\text{CO}_3\cdot 1.5\text{H}_2\text{O}$ can be identified. In all three samples the KCl exhibited the most intense peak, besides the minor OH-containing phases. The X-ray diffractograms within each series are

fairly similar and show the same tendency, unfortunately the water retention is uniformly traceable. Regarding chloride components, LiCl, NaCl and KCl were used as precursors, and it might be possible that not all the whole amount of the precursor chlorides was used up during the reaction.

Raman spectra of oxy-chloride samples were studied at higher wavenumber range and are discussed based on the number of observed bands, their positions and relative intensities.

Figure 2 shows the measured Raman spectra of the three sample series in the wavenumber range between 3300 cm^{-1} and 4000 cm^{-1} , which corresponds to the spectral region of the O-H stretching vibrations [14, 15].

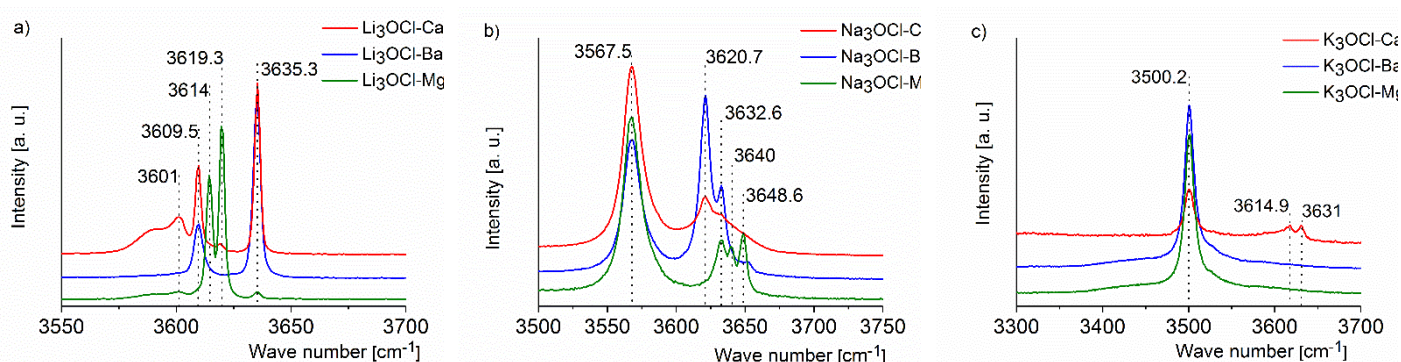


Figure 2. Raman spectra of $\text{Li}_3\text{OCl-Ca/Ba/Mg}$ (a), $\text{Na}_3\text{OCl-Ca/Ba/Mg}$ (b) and $\text{K}_3\text{OCl-Ca/Ba/Mg}$ (c) samples.

In case of Li-sample series, the $\text{Li}_3\text{OCl-Ca}$ and $\text{Li}_3\text{OCl-Ba}$ has a similar spectrum, exhibiting two well defined bands at 3635.3 cm^{-1} corresponds to O-H stretching and the band at 3609.5 cm^{-1} , related to the water presence. The Raman band shapes and intensities vary significantly with the compositions. In the spectra of $\text{Li}_3\text{OCl-Mg}$ the band positions and intensities are quite different from Ca and Ba doped samples, which implies different local environment, predicting another incorporation way of the doping-Mg element. The two sharp Raman bands in the spectrum of $\text{Li}_3\text{OCl-Mg}$ at 3614 cm^{-1} and at 3619.3 cm^{-1} are assigned to the O-H stretching vibration of the hydroxyl ion $\nu(\text{OH}^-)$. The Raman spectra of the $\text{Na}_3\text{OCl-Ca/Ba/Mg}$ samples also displays two broad contributions. A broadening symmetric band at 3567.5 cm^{-1} is present in all three samples connected to water. A multi-band distribution appears at higher wavenumbers with different intensities between 3620.7 cm^{-1} to 3648.6 cm^{-1} , due to the vibration of O-H. By changing the doping elements, band characteristics also change: the O-H stretching band becomes narrower in case of $\text{Na}_3\text{OCl-Ba}$ and wider in case of $\text{Na}_3\text{OCl-Mg}$, suggesting local rearrangements due to the addition of Ca/Ba or Mg. In case of the $\text{K}_3\text{OCl-Ca/Ba/Mg}$ samples there is a sharp Raman band at 3500.2 cm^{-1} , assigned to the water. The water band is most intense for $\text{K}_3\text{OCl-Ba}$ and $\text{K}_3\text{OCl-Mg}$ samples. In case of the $\text{K}_3\text{OCl-Ca}$ sample, O-H stretching band is observed at 3614.9 cm^{-1} and 3631 cm^{-1} whereas no such band can be observed in case of Ba and Mg doped samples.

During the XRD measurements and Raman spectroscopy investigations, the samples were kept in the air – although not for long period of time and in case of XRD, were covered by sticky tape - but due to the strong hygroscopic behavior of the samples, mainly the effect of incorporated water and CO_2 could be detected. Figure 1 and 2 are dominated by OH- and

water-connected phases. Therefore, bulk (neutron diffraction and DTA) and vacuum (TEM) methods were applied to characterize the samples and prevent water uptake.

Figure 3 shows neutron structure factors, $S(Q)$'s, of the investigated samples. The profiles are different from the X-ray diffraction profiles, since the scattering ability of the constituent elements are different for X-rays and neutrons. Significant differences can be observed between the different sample series, but within a series the character of the spectra is similar. Due to the characteristic features of the $S(Q)$ pattern, the main question is, how the atomic parameters help to understand the basic structure.

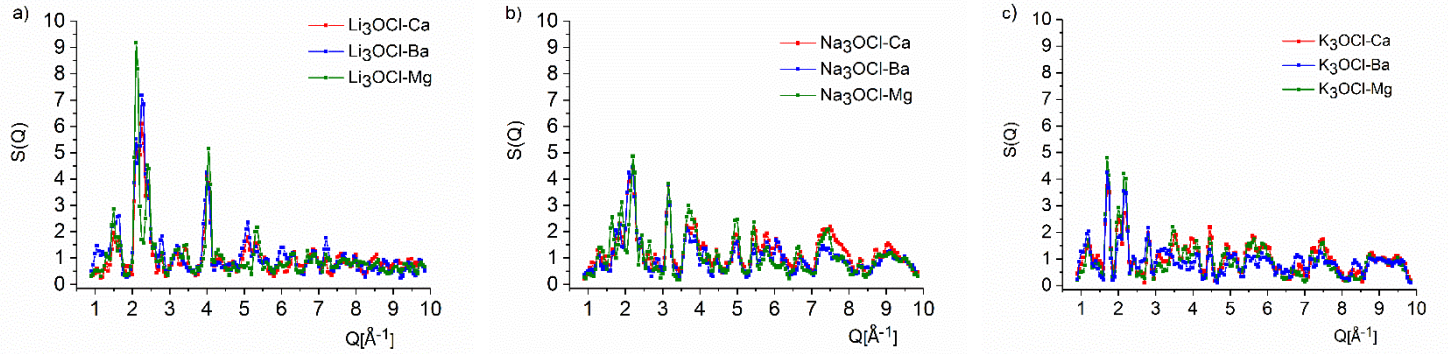


Figure 3. Total structure factors for $\text{Li}_3\text{OCl-Ca/Ba/Mg}$ (a), for the $\text{Na}_3\text{OCl-Ca/Ba/Mg}$ (b) and for the $\text{K}_3\text{OCl-Ca/Ba/Mg}$ (c) samples.

While from X-ray diffraction we obtained mixed phases, in case of neutron diffraction amorphous phases can be identified as indicated by the broad distributions (the crystalline phases are also present). Although it is not a pure amorphous state, we applied Reverse Monte Carlo [16] simulation technique for neutron diffraction measurements to investigate the atomic parameters of Ca-doped samples ($\text{Li}_3\text{OCl-Ca}$, $\text{Na}_3\text{OCl-Ca}$, $\text{K}_3\text{OCl-Ca}$). The starting procedure of the simulation were discussed in our previous study [17]. For the RMC starting model a random atomic configuration was built up with a simulation box containing 10 000 atoms with density data 0.045, 0.044 and 0.042 $\text{atoms}\cdot\text{\AA}^{-3}$ and half-box values $r_{\text{max}}=30.28$ \AA , 30.29 \AA and 30.32 \AA for the $\text{Li}_3\text{OCl-Ca}$, $\text{Na}_3\text{OCl-Ca}$ and $\text{K}_3\text{OCl-Ca}$ samples, respectively. In the RMC simulation procedure constraints have been used for the minimum interatomic distances between atom pairs (cut-off distances) to avoid unreasonable atom contacts. The characteristic features of the samples may be interpreted by taking into consideration the different weighting factors, w_{ij} of the partial structure factors, $S_{ij}(Q)$ contributing to the total $S(Q)$. In this work the following formalism is used:

$$S(Q) = \sum_{i,j}^k w_{ij} S_{ij}(Q), \quad (1)$$

$$w_{ij} = \frac{c_i c_j b_i b_j}{\left[\sum_{i,j}^k c_i b_j \right]^2} \quad (2)$$

where c_i , c_j are the molar fractions of the components, b_i , b_j the coherent neutron scattering amplitude [18] and k is the number of elements in the sample. **Table 1** contains the input parameters, the weighting factors for the atomic pairs, w_{ij} used in the RMC run for the Ca-doped samples.

Table 1. Neutron diffraction weighting factors of the partial interatomic correlations in the investigated samples.

Samples	Weighting factor, w_{ij} (%)									
	Li-Li	Li-Ca	Li-Cl	Li-O	Ca-Ca	Ca-Cl	Ca-O	Cl-Cl	Cl-O	O-O
Li₃OCl-Ca	31.84	-2.67	-107.93	-65.93	0.05	4.52	2.76	91.47	111.74	34.13
	Na-Na	Na-Ca	Na-Cl	Na-O	Ca-Ca	Ca-Cl	Ca-O	Cl-Cl	Cl-O	O-O
Na₃OCl-Ca	16.64	0.73	29.53	18.04	0.08	0.64	0.39	13.10	16.00	4.85
	K-K	K-Ca	K-Cl	K-O	Ca-Ca	Ca-Cl	Ca-O	Cl-Cl	Cl-O	O-O
K₃OCl-Ca	16.86	0.74	29.60	18.08	0.07	0.60	0.38	12.98	15.85	4.84

Thanks to the different neutron scattering length, it can be seen that the weighting factors for the Li₃OCl-Ca samples are very different than Na₃OCl-Ca and K₃OCl-Ca samples. Different atom pairs have significant contribution in the ND experiment for the Li- and for the Na- and K-based compositions. The convergence of the RMC calculation was good and the final $S(Q)$ matched very well with the experimental structure factor as it is shown in **Figure 4**.

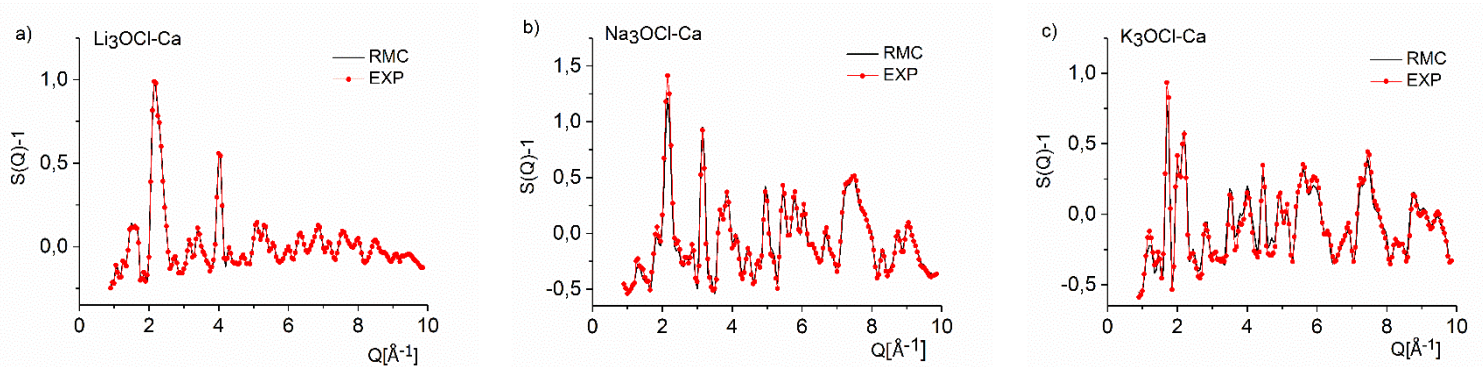


Figure 4. Neutron diffraction structure factor, $S(Q)$ of the Li₃OCl-Ca/Ba/Mg (a), for the Na₃OCl-Ca/Ba/Mg (b) and for the K₃OCl-Ca/Ba/Mg (c) samples, experimental data (red marks) and RMC simulation black solid.

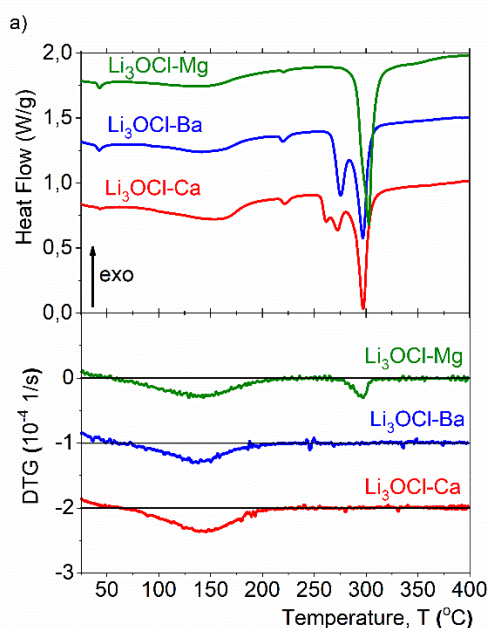
For the studied samples we have found very compact structures with characteristic first and second neighbor distributions (**Table 2**), which predict that even it's not a perfect structural configuration, the atomic connections are in the range of literature dates. The Li-Cl distance appears at 2.30 Å and K-Cl at 3.00 Å, both distances are shorter but close to the distances obtained to (Li,K)Cl mixture [19]. For the Na-Cl atomic pair correlations a well-defined first neighbor distance is obtained at 2.65 Å which is shorter than reported for the NaCl-liquid water solution in Ref. [20]. The most common distances in the three samples are Ca-O, Cl-O and Cl-Cl atomic pair correlations, we could check how they change with the compositions.

Table 2. First and second neighbour distances, r_{ij} (Å) for the different atom pairs. The actual error is indicated in bracket (Å), as estimated from the data analyses of different RMC runs.

Samples	Interatomic distances, r_{ij} (Å)									
	Atom pairs									
	Li-Li	Li-Ca	Li-Cl	Li-O	Ca-Ca	Ca-Cl	Ca-O	Cl-Cl	Cl-O	O-O
	(±0.03)	(±0.05)	(±0.03)	(±0.02)	Ca-Ca	(±0.05)	(±0.05)	(±0.03)	(±0.02)	(±0.03)

Li₃OCl-Ca	2.10	2.20	2.30/2.90	1.80/2.32	-	2.55	2.30	2.80/3.25	1.75	2.50
	Na-Na (±0.02)	Na-Ca (±0.04)	Na-Cl (±0.03)	Na-O (±0.02)	Ca-Ca	Ca-Cl (±0.05)	Ca-O (±0.05)	Cl-Cl (±0.03)	Cl-O (±0.02)	O-O (±0.03)
Na₃OCl-Ca	2.55	2.50	2.65/3.65	2.00	-	2.65	2.30/2.60	2.85/3.4	1.72	2.70
	K-K (±0.03)	K-Ca (±0.02)	K-Cl (±0.03)	K-O (±0.02)	Ca-Ca	Ca-Cl (±0.03)	Ca-O (±0.02)	Cl-Cl (±0.03)	Cl-O (±0.02)	O-O (±0.03)
K₃OCl-Ca	2.70	2.35	3.00/3.60	2.76	-	2.50	2.35	2.95/3.55	1.70	2.70

Even the doping Ca is in lowest concentration, we could find a relative sharp peak for Ca-O at 2.30 Å (for Li₃OCl-Ca and Na₃OCl-Ca) and at 2.35 Å (in K₃OCl-Ca sample), which are in agreement with the most results on Ca-based glasses [21, 22]. The Cl-O first neighbor distance shows slight concentration dependence, it changes from 1.75 Å, 1.72 Å to 1.70 Å from Li→Na→K, and is in good agreement with results reported for Cl₂O/ClO₂ in Ref. [23]. Significant atomic correlations have been established from the second neighbor distribution functions, as tabulated in Table 2, which emphasizes a strong correlated structure, where the Li-Li, Na-Na and K-K second neighbor distances show a sharp peak at relative short distances at 2.10 Å, 2.55 Å and 2.70 Å, respectively. The Li-Cl, Na-Cl and K-Cl correlation functions show two well defined peaks at 2.30/2.90 Å, 2.65/3.65 Å and 3.00/3.60 Å, respectively. The Cl-Cl correlation functions consist of double peaks, both distances increase slightly as function of increasing ionic radius of the alkali component, from 2.80/3.25 Å (Li), 2.85/3.4 Å (Na) to 2.95/3.55 Å (K). From the RMC modeling we can conclude that the first neighbor pair correlations indicate that Ca incorporated in the Li-, Na- and K-based network units. Structural changes, including melting, were observed with a thermal analysis approach. **Figures 5** a-c shows the heat flow and DTG (normalized weight loss rate) curves for the Li₃OCl-Ca/Ba/Mg, for the Na₃OCl-Ca/Ba/Mg and for the K₃OCl-Ca/Ba/Mg samples, respectively.



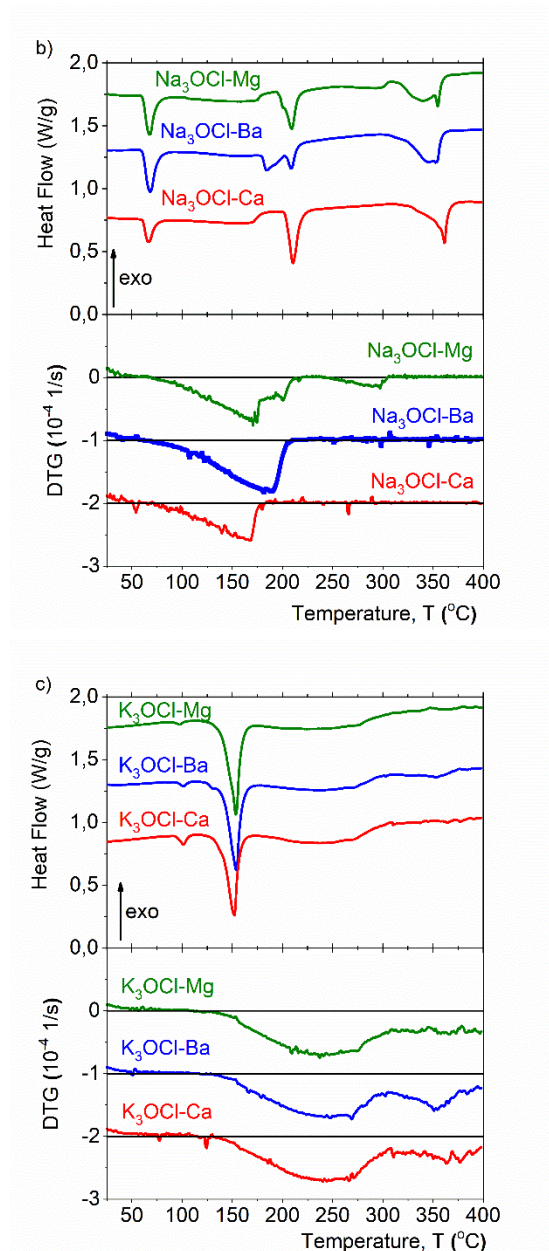


Figure 5. Heat flow and DTG curves for $\text{Li}_3\text{OCl-Ca/Ba/Mg}$ (a), for the $\text{Na}_3\text{OCl-Ca/Ba/Mg}$ (b) and for the $\text{K}_3\text{OCl-Ca/Ba/Mg}$ (c) samples.

For each heat flow and DTG diagram, the curves were shifted arbitrarily along the vertical axis. Onset temperatures of the endothermic peaks are summarized in **Table 3**.

Table 3. Onset temperatures of the endothermic events and the peak temperature for weight loss rate.

Sample	$T_{1 \text{ onset}} (^{\circ}\text{C})$	$T_{2 \text{ onset}} (^{\circ}\text{C})$	$T_{3 \text{ onset}} (^{\circ}\text{C})$	$T_{\text{DTG peak}} (^{\circ}\text{C})$
$\text{Li}_3\text{OCl-Ca}$	40.9	217.4	256.8, 258.9, 287.1	143
$\text{Li}_3\text{OCl-Ba}$	38.6	216.6	266.8, 285.8	138
$\text{Li}_3\text{OCl-Mg}$	39.5	217.5	289.5	142 and 297

Na ₃ OCl-Ca	60.8	203	311-352	169
Na ₃ OCl-Ba	60.7	203	302-360	191
Na ₃ OCl-Mg	60.7	196.9, 199	316-349	173 and 295
K ₃ OCl-Ca	93.5	139.6	–	242
K ₃ OCl-Ba	95.5	140.6	–	245 and 363
K ₃ OCl-Mg	91.7	138.0	–	237 and 352

For the Li₃OCl samples, the onset temperatures around 290 °C indicate the presence of Li₃OCl phase. The total relative weight losses during the room temperature (RT) to 400 °C heat treatment for all the investigated Li₃OCl-Ca/Ba/Mg, Na₃OCl-Ca/Ba/Mg and K₃OCl-Ca/Ba/Mg samples are summarized in **Figure 6**. Weight loss in the investigated samples causes thermal effects, which effects can be observed as broad endothermic events along the heat flow curves (cf. the DTG and heat flow curves). Based on the work [24], the endothermic peaks at about 40 °C together with the broad endothermic (weight loss) events in Figure 5a (up to ca. 200 °C) are probably caused by phase change and gradual decomposition of a Li₂OHCl phase. This hydroxide phase may have formed incidentally due to the presence of water vapor during the experimental procedure. The peak of a similarly broad thermal event was reported as an indication for glass transition in Ref [25].

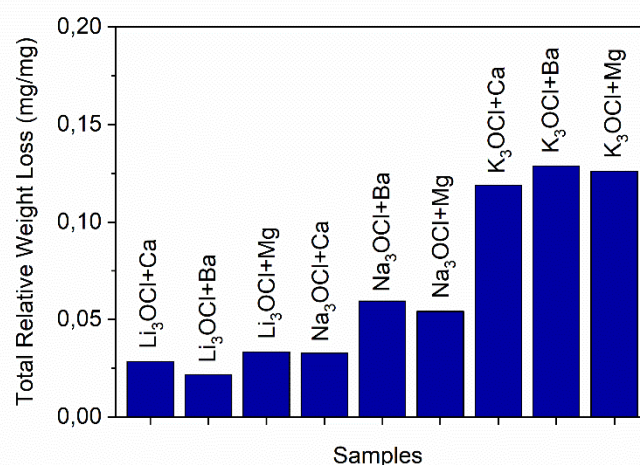


Figure 6. Total relative weight loss of the different Li₃OCl-Ca/Ba/Mg, Na₃OCl-Ca/Ba/Mg and K₃OCl-Ca/Ba/Mg samples.

For comparison, the approximate peak temperatures of weight loss rate are also listed in Table 3. The subsequent endothermic peaks with onset temperatures around 217 °C, 260 °C and above 270 °C are reported as a phase changes and subsequent melting of the Li₃OCl phase [26]. However, based on the work in Ref [13] the peak with onset temperature at 270 °C (peak temperature just below 300 °C) corresponds to the melting of the Li₂OHCl phase while the larger peak with onset temperature at about 290 °C is related to the melting point of the Li₃OCl phase [13].

Weight loss starts at higher temperatures (above 130-140 °C) in K₃OCl samples than in the similar Li₃OCl (68-75 °C) and Na₃OCl (75-83 °C) samples. This 130-140 °C range is in

coincidence with the main endothermic peak of the K_3OCl samples, which indicates that total melting of the K_3OCl samples takes place at this temperature and the melting triggers the weight loss process. Calculating the magnitude of the weight loss relative to the sample mass, K sublimation from molten structure cannot be excluded for the K_3OCl samples, therefore, the total relative weight loss in the K_3OCl samples is significantly larger than in Li- and Na-based samples and it extends to a broader temperature range as well. For Na_3OCl samples, the endothermic events with onset temperatures at around 60 °C and 360 °C might correspond to the melting of water free and water containing NaOH phases, respectively. In these samples weight loss starts after the first endothermic events and it finishes at the second endothermic event. A second, minor weight loss event can also be observed for the samples with Mg addition in both Li_3OCl and Na_3OCl , which may indicate the formation and dehydration of a water containing $MgCl_2$ phase in these samples during the DTA analysis.

As both the thermal properties and diffraction results indicated nanoscale inhomogeneities in the network structure, an attempt was made to directly prove the presence of these inhomogeneities using local analytical methods by performing TEM investigations. The nanocrystallinity has been confirmed by a set of measurements on several samples, which indicated that the samples exhibit structural and compositional inhomogeneities on the nanometer scale.

The Li_3OCl -Ca/Ba/Mg samples have similar morphologies, these samples are dominantly composed of 50-70 nm sized grains, however, 200-500 nm sized grains also occur (**Figure 7** a-b).

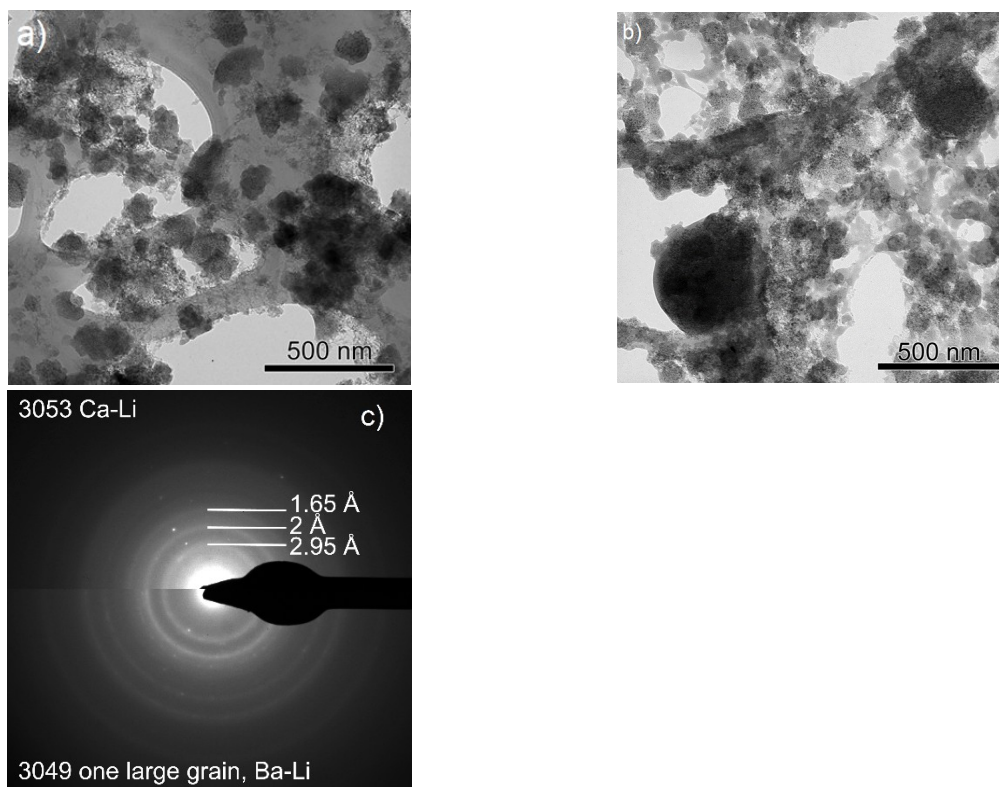


Figure 7. Morphologies of the Li_3OCl -Ca/Ba samples, TEM image of Li_3OCl -Ca (a), Li_3OCl -Ba (b) and SAED patterns of the Li_3OCl -Ca (top) and -Ba (bottom) (c).

On the SAED patterns measured on these samples several diffuse diffraction rings can be observed, indicating a poorly ordered but not completely amorphous structure. Figure 7c

shows a SAED pattern taken from an aggregate of ca. 1 micrometer of diameter of the Ca-Li sample together with another pattern taken from ca. 250 nm sized area of a larger grain of the Ba-Li sample. The diffraction rings of the two SAED patterns not always equally continuous, but as their positions coincide indicating similar lattice spacings, structural similarity have concluded. In these samples, based on EDS measurements, no compositional inhomogeneities were observed, the O:Cl ratio approximates 1:1.

Based on morphology, diffraction pattern and composition, three phases were identified in the Na_3OCl -Ca sample: Na-O, Ca-O phases, with little chlorine and cubic NaCl. In agreement with the XRD, the Na_3OCl -Ba sample contains amorphous sites and Ba-O nanoparticles, with 100-150 nm crystallite size. In the Na_3OCl -Mg sample, nanoparticles containing Mg and Na can be identified in the amorphous matrix (see **Figure 8**). The elemental maps in Figure 8 show that Mg is hosted by the Cl and Na containing phase.

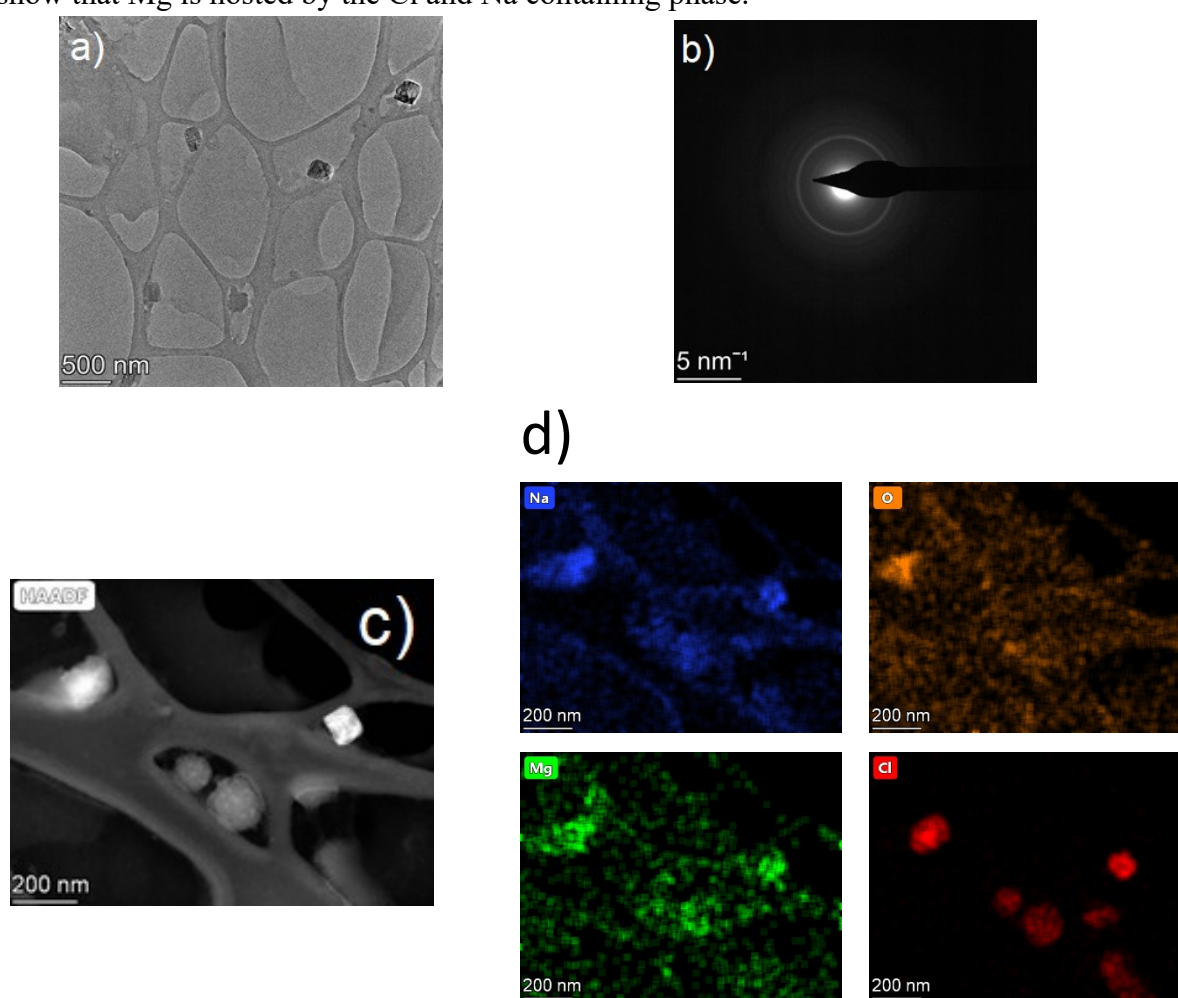


Figure 8. Morphologies of the Na_3OCl -Mg sample, TEM image (a), SAED pattern (b), HAADF image (c) and elemental mapping images (d) of Na, O, Mg and Cl components.

In the K-based samples spherical inhomogeneities are seen in the amorphous matrix. In the K_3OCl -Ca sample, Ca can be found in larger, more than 100 nm sized grains and it also forms a phase with Cl and O. In the K_3OCl -Ba sample, Ba-O nanoparticles can be identified in the amorphous matrix and Ba is present in the form of nanocrystals with a particle size below <100 nm. In the K_3OCl -Mg sample elongated needle-shaped K-O-Cl-Mg crystals with

micrometer length can be identified together with several 100 nm large panel-shaped K-O-Mg-Cl crystals. The separation of the doping elements can be observed in all samples. For example, in case of $\text{K}_3\text{OCl-Ba}$ sample, EDS mapping demonstrated that Ba nanoparticles are present mainly in amorphous phase (see **Figure 9**). Elemental maps indicate that Ba is present in form of oxide.

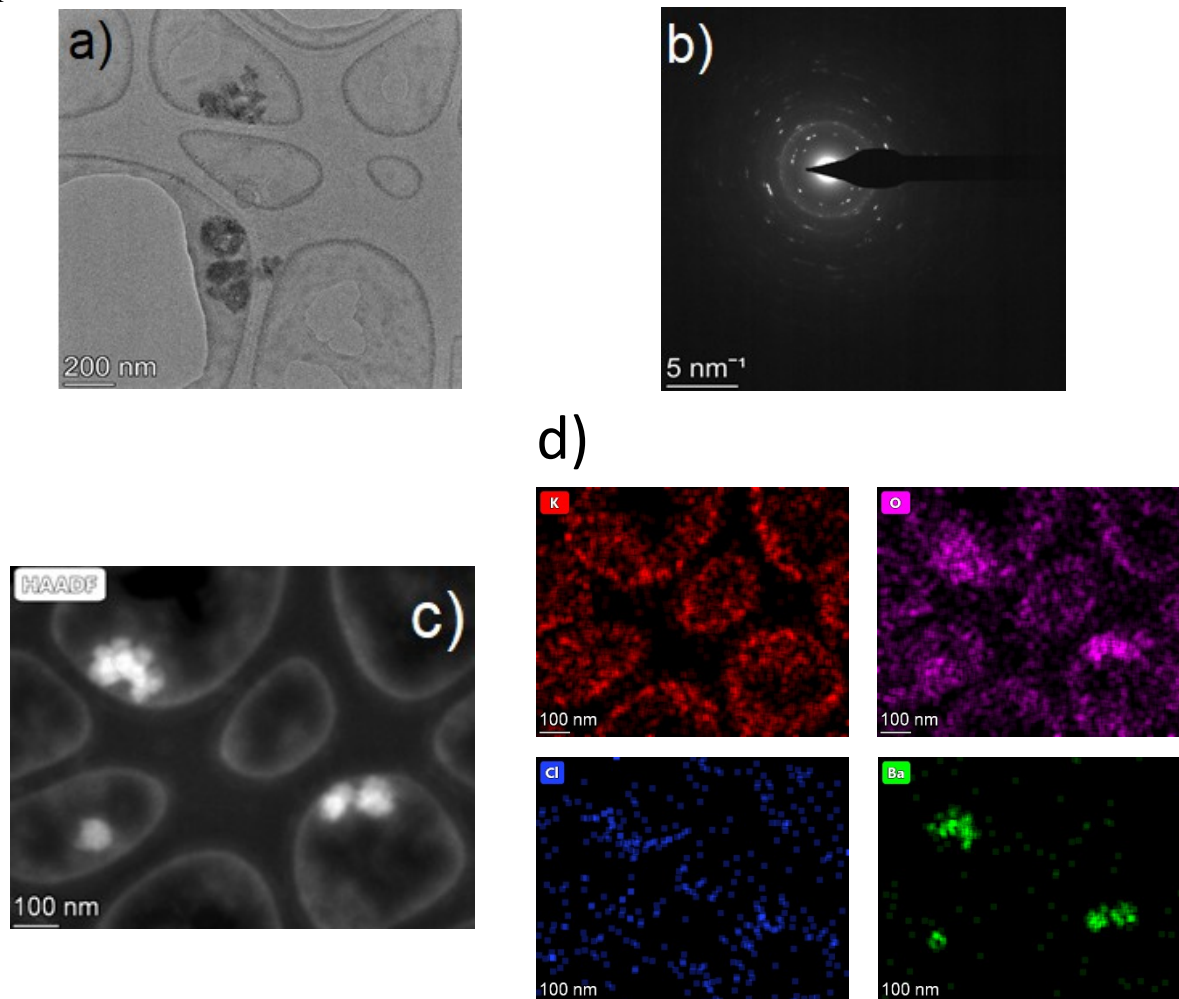


Figure 9. Morphologies of the $\text{K}_3\text{OCl-Ba}$ sample, TEM image (a), SAED pattern (b), HAADF image (c) and elemental mapping images (d) of K, O, Cl and Ba components.

The ionic conductivity of the solid electrolytes is lower than that of the liquid electrolytes, therefore it is needed to enhance the conductivity of the solids. The Li-ion batteries can reach as high ionic conductivity as 10^{-3} - 10^{-2} S cm^{-1} at RT.

The ionic conductivity at RT changed from 6.05×10^{-6} S cm^{-1} to 1.5×10^{-6} S cm^{-1} from $\text{Li}_3\text{OCl-Mg}$ \rightarrow $\text{Li}_3\text{OCl-Ba}$ \rightarrow $\text{Li}_3\text{OCl-Ca}$, which are lower than expected for several Li-based samples [27, 28] but higher than the ceramic Li_3OCl sample (5.8×10^{-7} S cm^{-1}) [29]. The Na-based solid electrolytes exhibit ionic conductivity around 1.8 - 2.0×10^{-6} S cm^{-1} which is significantly lower than in cases of well-known NASICON compositions [30, 31]. The ionic conductivity of the K-samples were 1.1 - 1.6×10^{-6} at room temperature, and this value is under the expectation based on Ref [32, 33].

4. Conclusions

Thermal and structural characteristics of three oxy-chlorite systems Li_3OCl , Na_3OCl and K_3OCl were investigated as function of Ca, Ba and Mg doping elements. The structural characterization of the samples by neutron and X-ray diffractometry, subsequent thermal, Raman and TEM studies suggest that the synthesized material is a mixture of amorphous and crystalline phases. From X-ray diffractometry, we could successfully identify the Li_3OCl anti-perovskite phase for all the Ca-, Ba- and Mg-doped samples. The XRD phase analysis and Raman spectra prove that the samples absorb water. Neutron diffraction measurements on 100°C indicated a mixed state of the phases in the samples, besides the Bragg-peaks of the crystalline phases, the typical broad distributions supported the presence of amorphous phase. From Reverse Monte Carlo simulation, we identified the first- and second-neighbour distances in case of Ca-doped samples and supported that the Ca atom is incorporated in the main Li, Na, K-based structure. Thermal stability of the samples increases as follows: $\text{K}_3\text{OCl} > \text{Na}_3\text{OCl} > \text{Li}_3\text{OCl}$. Investigations on the submicrometer scale supports the presence of nanograins, structural and compositional inhomogeneities on the nanometer scale. The elemental mapping indicates that Mg is incorporated into Cl- and Na-bearing phase in case of the Na_3OCl -Mg sample and the Ba is present in the form of oxide nanoparticles in case of the K_3OCl -Ba sample.

The ionic conductivity was determined to be in the range of $1.1\text{-}6 \times 10^{-6} \text{ S cm}^{-1}$ for all Li-, Na- and K-based samples, which indicates need for improvement in the fields conductivity and perhaps the sample preparation way.

Acknowledgement – Indo-Hungary research project supported by NRIDO, Hungary and DST, India and Grant Nr. 2017-2.3.7-TÉT-IN-2017-00023. ZsK's work was completed in the ELTE Institutional Excellence Program (TKP2020-IKA-05) financed by the Hungarian Ministry of Human Capacities. HRTEM facility at Centre for Energy Research was granted by the European Structural and Investment Funds, grant no. VEKOP-2.3.3-15-2016-00002.

Conflict of Interest

The authors declare no conflict of interest.

References

- [1] M. H. Braga, C. M. Subramaniam, A. J. Murchison, *J. Am. Chem. Soc.* **2018**, 140(20), 6343-6352.
- [2] M. H. Braga, J. A. Ferreira, A. J. Murchison, J. B. Goodenough, *J. Electrochem. Soc.* **2017**, 164, A207-A213.
- [3] J. B. Goodenough, H. M. Braga, *Dalton Transactions*, **2017**, DOI: 10.1039/c7dt03026f
- [4] Z. Zhang, Y. Shao, B. Lotsch, Y-S. Hu, H. Li, J. Janek, L. F. Nazar, C-W. Nan, J. Maier, M. Armand, L. Chen, *Energy & Enc. Science*, **2018**, DOI: 10.1039/c8ee01053f.
- [5] J. C. Bachman, S. Mui, A. Grimaud, H-H. Chang, N. Pour, S. F. Lux, O. Paschos, F. Maglia, S. Lupart, P. Lamp, L. Giordano, Y. Shao-Horn, *Chem. Rev.*, **2016**, 116, 140-162.
- [6] B. Wu, S. Wang, W. J. Evans, D. Z. Deng, J. Yang, J. Xiao, *J. Mat. Chem. A*, **2016**, DOI: 10.1039/C6TA05439K.
- [7] A. Emly, E. Kioupakis, A. V. der Ven, *Chem. Mat.*, **2013**, 25, 4663-4670.

- [8] J. B. Goodenough, P. Singh, *J. Electrochem. Soc.*, **2015**, 162, A2387-A2392.
- [9] C. Julien, A. Mauger, A. Vijn, K. Zaghib, *Lithium Batteries: Science and Technology*, **2015**, Springer, ISBN 978-3-319-19108-9.
- [10] X.-Q. Zhang, X. Chen, R. Xu, X.-B. Cheng, H.-J. Peng, R. Zhang, J.-Q. Huang, Q. Zhnag, *Angew. Chem. Int. Ed.*, **2017**, 56, 14207-14211.
- [11] M. H. Braga, A. J. Murchison, J. A. Ferreira, P. Singh, J. B. Goodenough, *Energy & Env. Sci.*, **2015**, DOI: 10.1039/c5ee02924d
- [12] E. Svab, G. Meszaros, F. Deak, *Mater. Sci. Forum*, **1996**, 228, 247-252.
- [13] S. Li, J. Zhu, Y. Wang, J. W. Howard, X. Lü, Y. Li, R. S. Kumar, L. Wang, L. L. Daemen, Y. Zhao, *Solid State Ionics*, **2016**, 284, 14-19.
- [14] J. Stefanski, C. Schmidt, S. Jahn, *Phys. Chem. Chem. Phys.*, **2018**, 20, 21629-21639.
- [15] M. Ahmed, A. K. Singh, J. A. Mondal, *Phys. Chem. Chem. Phys.*, **2016**, 18, 2767-2775.
- [16] O. Gereben, P. Jovari, L. Temleitner, L. Pusztai, *J. Optoelect. Adv. Mat.*, **2007**, 9, 3021-3027.
- [17] M. Fabian, E. Svab, Th. Proffen, E. Veress, *J. Non-Cryst. Solids*, **2008**, 354, 3299-3307.
- [18] A. C. Hannon, ISIS Disordered Materials Database, **2006**,
<http://www.wisis2.isis.rl.ac.uk/Disordered/Database/DBMain.htm>, available at 11.01.2020.
- [19] Y. Miyamoto, S. Okazaki, O. Odawara, I. Okada, M. Misawa, T. Fukunaga, *Mol. Physics*, **1994**, 82, 887-895.
- [20] J. M. Khalack, A. P. Lyubartsev, *Cond. Matt. Physics*, **2004**, 7, 683-698.
- [21] L. F. Chungong, L. A. Swansbury, G. Mountjoy, A. C. Hannon, A. F. Lee, R. A. Martin, *Appl. Sci. Glass.*, **2017**, 8, 383-390.
- [22] M. Fabian, Zs. Kovacs, J- L. Labar, A. Sulyok, Z. E. Horvath, I. Szekacs, V. K. Kis, *J. Mater. Sci.*, **2020**, 55, 2303-2320.
- [23] J. D. Dunitz, K. Hedberg, Contribution No. 1384 from The Gates and Crellin Laboratories of Chemistry, California Institute of Technology, **1950**, 72, 3108-3112.
- [24] I. Hanghofer, G.J. Redhammer, S. Rohde, I. Hanzu, A. Senyshyn, H.M.R. Wilkening, D. Rettenwander, *Chem. Mater.* **2018**, 30, 8134–8144.
- [25] M. H. Braga, J. A. Ferreira, V. Stockhausen, J. E. Oliveira, A. El-Azab, *J. Mater. Chem. A*, **2014**, 2, 5470-5480.
- [26] A. Y. Song, Y. Xiao, K. Turcheniuk, P. Upadhyaya, A. Ramanujapuram, J. Benson, A. Magasinski, M. Olguin, L. Meda, O. Borodin, G. Yushin, *Adv. Energy Mater.* **2018**, 8, 1700971.
- [27] J. Zhu, S. Li, Y. Zhang, J. W. Howard, X. Lü, Y. Li, Y. Wang, R. S. Kumar, L. Wang, Y. Zhao, *Appl. Phys. Lett.* **2016**, 109, 101904.
- [28] X. Lü, J. W. Howard, A. Chen, J. Zhu, S. Li, G. Wu, P. Dowden, H. Xu, Y. Zhao, Q. Jia, *Adv. Sci.* **2016**, 3, 1500359.
- [29] X. Lü, G. Wu, J. W. Howard, A. Chen, Y. Zhao, L. L. Daemen, Q. Jia, *Chem. Commun.* **2014**, 50, 11520-11522.
- [30] R. Supriya, K.P. Padma, *Sol. Stat. Ion.* **2013**, 253, 217-222.
- [31] J. W. Fergus, *Sol. Stat. Ion.* **2013**, 227, 102-112.
- [32] R.D. Bayliss, S.N. Cook, S. Fearn, J.A. Kilner, C. Greaves, S.J. Skinner, *En. & Env. Sci.* **2014**, 7, 2999-3005.

[33] H. Yuan, H. Li, T. Zhang, G. Li, T. He, F. Du, S. Feng, *J. Mat. Chem. A* **2018**, 6, 8413-8418.

Margit Fabian^{1*}, Istvan Tolnai¹, Atul Khanna², Zsolt Endre Horvath¹, Viktoria Kovacs Kis¹, Zsolt Kovacs³

Structural Characterization of Oxy-Halide Materials for Solid State Batteries

Novel Ca, Ba, Mg doped Li_3OCl , Na_3OCl and K_3OCl oxy-halides have been synthesized. The formation of anti-perovskite Li_3OCl is verified by X-ray diffractometry. Raman spectra show that the samples absorb water. From Reverse Monte Carlo simulation, the first- and second-neighbour distances can be identified in case of Ca-doped samples, approving the short-range order. The Li_3OCl samples are the most thermally stable series. TEM investigations indicate that the samples exhibit structural and compositional inhomogeneities on the nanometer scale.

